HHS Public Access

Author manuscript

J Opt Soc Am A Opt Image Sci Vis. Author manuscript; available in PMC 2020 March 18.

Published in final edited form as:

J Opt Soc Am A Opt Image Sci Vis. 2020 March 01; 37(3): 374–383. doi:10.1364/JOSAA.380925.

Effect of tilt on circular zone plate performance

Sajid Ali[1], **Chris Jacobsen**[2,3,4,*]

[1]Applied Physics, Northwestern University, Evanston, Illinois 60208, USA

[2]Advanced Photon Source, Argonne National Laboratory, Argonne, Illinois 60439, USA

[3]Department of Physics & Astronomy, Northwestern University, Evanston, Illinois 60208, USA

[4]Chemistry of Life Processes Institute, Northwestern University, Evanston, Illinois 60208, USA

Abstract

Fresnel zone plates are frequently used as focusing and imaging optics in x-ray microscopy, as they provide the ease of use of normal incidence optics. We consider here the effects of tilt misalignment on their optical performance, both in the thin optics limit and in the case of zone plates that are sufficiently thick that volume diffraction effects come into play. Using multislice propagation, we show that simple analytical models describe the tilt sensitivity of thin zone plates and the thickness at which volume diffraction must be considered, and examine numerically the performance of example zone plates for soft x-ray focusing at 0.5 keV, and hard x-ray focusing at 10 keV.

1 Introduction

Fresnel zone plates are widely employed as focusing and imaging optics in x-ray microscopy [1, 2, 3]. One important characteristic of a Fresnel zone plate is its finest, outermost zone width dr_N which limits the Rayleigh spatial resolution to $\delta_r = 1.22 dr_N/m$ [4, 5] for the m^{th} diffraction order. Another is its thickness t_{zp}, which limits the diffraction efficiency for x-ray focusing [6]. Ideally the thickness should approach a value of

$$t_{\text{zp,opt}} \simeq \frac{\lambda}{2\delta}\left(1 - \frac{2\beta}{\pi\delta}\right) \tag{1}$$

so that the zones impart a phase shift of approximately π on the wave exiting the zone plate. The expression of Eq. 1 assumes $\beta \ll \delta$, where δ as the phase shifting part, and β as the absorptive part, of the x-ray refractive index of

$$n = 1 - \delta - i\beta \tag{2}$$

when using $\exp[-ikz]$ for forward wave propagation. Values of δ and β are typically well below 10^{-2} [7]. Zone plates used for efficient sub-1 keV x-ray focusing should have values

*corresponding author.

Disclosures

The authors declare no conflicts of interest.

of t_{zp} of ~ 100–200 nm, while those used for 10 keV x-ray focusing should have values of t_{zp} of more like 1–2 μm. Therefore a Fresnel zone plate's maximum aspect ratio AR = t_{zp}/dr_N is an important characteristic. Advances in nanofabrication methods have enabled the fabrication of zone plates with sub-10 nanometer outermost zone width, and corresponding spatial resolution for imaging high contrast features [8, 9, 10]. At the same time, aspect ratios exceeding 50:1 have been achieved in single zone plates [11, 12, 13], and on-chip stacking has provided another route for high aspect ratios [14].

Zone plates with high aspect ratios, and finest zone widths dr_N approaching the x-ray wavelength λ, have properties that begin to depart from those of thin zone plates. To maximize diffraction efficiency in thicker zones, the outermost zones ideally should be tilted relative to the incident beam direction by the Bragg angle θ_B [15, 3] of

$$\theta_B(r_n) = \frac{1}{2}\tan\left(\frac{r_n}{f}\right) \tag{3}$$

for the zone at a radius r_n, though this has yet to be achieved in practice. In addition, as the aspect ratio increases, one must begin to consider waveguide effects, with coupled wave theory offering one approach to calculate these effects at a particular radius under the assumption that the small variation in the width of nearby zones means that locally one can use the solution for an infinite linear grating [15]. Subsequent coupled wave equation studies have shown that the diffraction efficiency can be improved for specific values of x-ray wavelength λ, aspect ratio, and zone tilt [16, 17, 18, 19]. While coupled wave theory provides an analytical solution for an infinite, constant-period volume grating so that one gains insight for specific subregions of a zone plate, multislice propagation methods [20, 21] (also called the beam propagation method [22]) can be used to calculate the focusing properties of complete zone plates with volume diffraction effects included, as well as with fabrication errors accounted for [23, 24, 25, 26]. Thus the focusing properties of Fresnel zone plates in perfect optical systems are well understood.

However, not all microscopes employing Fresnel zone plates are perfect. One of the challenges is to align a zone plate so that it is truly perpendicular to the incident x-ray illumination. This is different than considering the tilt angle of zones at specific radii so as to achieve the Bragg condition of Eq. 3; instead, this tilt of the entire circular zone plate introduces aberrations in focusing. Simple analytical estimates for tilt limits have been obtained for thin zone plates [4, 27] as will be discussed below. However, apart from a brief summary of our early results [28], no systematic studies have been carried out to reveal the details of how the focal spot is degraded as a function of overall zone plate tilt, nor have volume diffraction effects for tilted, high aspect ratio zone plates been considered. We investigate this question so as to understand the tilt tolerances of Fresnel zone plates used for x-ray nanofocusing and nanoimaging, including in the case of hoped-for advances in finest zone width dr_N and thickness t_{zp}.

Zone plate tilting has been carried out in a deliberate fashion in specific prior studies. With a linear zone plate that focuses in only one direction, one can tilt the zone plate along the non-focusing direction in order to increase the projected thickness of the zone material and thus

increase the focusing efficiency at higher photon energies [29]. When extreme tilts are used, zone positions can be tapered along that direction so that zones at all distances from the desired focus position satisfy the one-dimensional version of Eq. 4 below [30]. Multilayer Laue lenses (MLLs) can be thought of as thick one-dimensional zone plates that can be used in orthogonal pairs for 2D focusing [31], and both their focal spot properties and focusing efficiency are affected by the tilt of each 1D optic compared to the desired Bragg condition, either for constant-thickness zones [32, 19] or for variable-thickness or wedged MLLs [33]. Our results here are instead for circular zone plates which provide 2D focusing in a single optic.

2 Analytical limits to the tilt of thin zone plates

A Fresnel zone plate with a focal length of f in first diffraction order has zone boundaries at radii

$$r_n^2 = n\lambda f + (\frac{n\lambda}{2})^2 \tag{4}$$

where n is the integer zone number (leading up to the outermost zone N), and the second term corrects for spherical aberration when focusing a plane wave. When the total number of zones N is large, one can approximate the outermost zone width dr_N as

$$dr_N = \frac{\lambda f}{2r_N}, \tag{5}$$

which allows one to obtain equivalent expressions of

$$N = \frac{r_N}{2dr_N} = \frac{\lambda f}{(2dr_N)^2}. \tag{6}$$

We now consider the case of wavefield aberrations produced by optical path length differences in tilted zone plates, using the geometry shown in Fig. 1. The path length difference $\mathscr{O}'_u$ between the upper marginal ray and the central axis [27, Eq. 10] is given by

$$\mathscr{O}'_u = r_N \sin(\theta) + f\left[1 + (\tan(\theta) - r_N / f)^2\right]^{1/2} - f\left[1 + \tan^2(\theta)\right]^{1/2} \tag{7}$$

We have also calculated the equivalent relationship for the lower marginal ray relative to the central axis, which is

$$\mathscr{O}'_l = r_N \sin(\theta) + f\left[1 + \tan^2(\theta)\right]^{1/2} - f\left[1 + (r_N / f + \tan(\theta))^2\right]^{1/2}. \tag{8}$$

These expressions can be simplified by expanding to first order in the tilt angle, and second order in the binomial approximation of the square roots, giving approximate results of

$$\ell_u = \left(\frac{r_N^2}{2f} - \frac{r_N^4}{8f^3}\right) + \frac{r_N^3}{2f^2}\theta - \frac{3r_N^2}{4f}\theta^2 = (\ell_0) + \ell_c\theta - \ell_a\theta^2 \tag{9}$$

and

$$\ell_l = (\ell_0) + \ell_c\theta + \ell_a\theta^2 \tag{10}$$

where the same terms ℓ_0, ℓ_c, and ℓ_a defined in Eq. 9 appear also in Eq. 10. The term ℓ_0 describes the wavefield converging to a focus (plus spherical aberration, which the second term in Eq. 4 corrects for), and is independent of tilt. The term ℓ_c describes coma, and the term ℓ_a describes astigmatism and field curvature (referred to below as astigmatism only).

As one can see from Eqs. 9 and 10, the coma term ℓ_c can compensate for the opposite-sign astigmatism term ℓ_a up to some tilt angle θ for the upper marginal ray relative to the axial ray, but in the case of the lower marginal ray both terms have the same sign. Therefore the overall tilt limit of the zone plate is best characterized by the lower marginal ray calculation of Eq. 10. The ratio of the astigmatism term $\ell_a\theta^2$ over the coma term $\ell_c\theta$ can be written as

$$\frac{\ell_a\theta^2}{\ell_c\theta} = \frac{3\theta}{2r_N / f} = \frac{3}{2}\frac{\theta}{\text{N.A.}} \tag{11}$$

where

$$\text{N.A.} = n\sin\left(\arctan\left(\frac{r_N}{f}\right)\right) \simeq \frac{r_N}{f} = \frac{\lambda}{2dr_N} \tag{12}$$

is the numerical aperture of the zone plate, which typically has quite small values (here one can use $n \simeq 1$ based on Eq. 2). Therefore the term that dominates in ℓ_l will depend on how the tilt angle compares with the zone plate's numerical aperture N.A..

Whichever term in the lower marginal ray calculation dominates, we can ask that it not exceed λ/4 so as to satisfy the Rayleigh quarter wave criterion for minimal aberrations in focusing. This gives rise to a tilt limit of

$$\theta_l : \ell_l < \frac{\lambda}{4} \tag{13}$$

If the first term $\ell_c\theta$ dominates (that is, $\theta \ll$ N.A.), we arrive at a tilt limit due to coma [27, Eq. 14] of

$$\theta_c < \frac{\lambda f^2}{2r_N^3} = \frac{1}{2N\,\text{N.A.}}. \tag{14}$$

If the second term $\ell_a\theta^2$ dominates (that is, if $\theta \gg$ N.A.), we arrive at a tilt limit due to astigmatism of [27, Eq. 13]

$$\theta_a < \sqrt{\frac{\lambda f}{3r_N^2}} = \sqrt{\frac{2}{3}\frac{dr_N}{r_N}} = \frac{1}{\sqrt{3N}} \tag{15}$$

where in both cases we have used Eqs. 4 and 6 to obtain two equivalent expressions. Examples of which term dominates, and the resulting limits on tilt angles, are shown in Fig. 2.

3 Approaches to simulating zone plate focal spots

With a thin untilted zone plate, one can take a forward traveling plane wave $\psi_0 \exp[-ikz]$ and modulate it by the transmission of the zone-containing regions of the optic. The modulation to the transmitted wave is

$$\psi = \psi_0 \exp[ik\delta t] \exp[-k\beta t] \tag{16}$$

using the x-ray index of refraction $n = 1 - \delta - i\beta$ given by Eq. 2, where $k = 2\pi/\lambda$ and t is the thickness of the material along the x-ray beam direction. One can then use free-space Fresnel propagation to bring the zone-plate-modulated exit wave to the plane of the focus. If this calculation is done using a discrete Cartesian grid with transverse voxel size Δ_x and longitudinal voxel size Δ_z, one must worry about aliasing effects with circular Fresnel zones. If a calculation grid voxel is fully filled with zone material, then one replaces t with Δ_z in Eq. 16. If, however, only a fraction χ of a calculation grid voxel is filled with zone material, one can make the substition $t \rightarrow \chi\Delta_z$ in Eq. 16 and obtain accurate results [25]. An example of this partial voxel filling approach for a zone plate with $t_{zp} < \Delta_z$ is shown in Fig. 3. One can obtain a good numerical approximation for χ by first calculating zero-or-one filling of zones on a much more finely sampled 2D array and then downsampling to the desired array size for subsequent calculations.

One has two options (Fig. 4) for carrying out the calculation of how a tilted zone plate modulates the incident plane wave to yield the wave exiting the zone plate:

- **Optic-aligned:** one approach is to work in a coordinate system aligned to the zone plate, and tilt the illumination by an angle θ as illustrated in Fig. 4A. If one uses numerical wave propagation with a 2D input grid of N_x pixels each of size Δ_x, the incident wave phase change per pixel φ_x is given by

$$\varphi_x = \frac{2\pi}{\lambda} x \tan(\theta) \tag{17}$$

  where x is the coordinate of the pixel along the axis of tilt. This is implemented by creating a matrix that contains φ_x values for each pixel, followed by pointwise application of this phase using $\exp(\varphi_x)$.

  If one uses a numerical wave propagation approach to take the exit wave to the m^{th} order focal plane where one has the same calculation grid pixel size Δ_x at the focal plane, one must limit the wavefield tilt angle to

$$\theta_f = \frac{mr_N}{f} = \frac{N_x \Delta_x}{2f} \tag{18}$$

in order to have the focus spot be within the calculation grid at the focal plane. The alternative is to increase the number of 2D pixels and thus surround the zone plate by a larger emptier area, but there are practical limits to array size N_x^2 as set by available computer memory if using a single compute node.

We note that there are other approaches to calculating wavefield propagation with tilted plane wave inputs [34, 35, 36]. We became aware of these alternative approaches only after our main calculations were completed, so we did not consider their properties for this work.

- **Wavefield-aligned:** an alternative approach is to use an incident plane wave aligned to a 3D calculation grid, and tilt the zone plate relative to the grid as shown in Fig. 4B. In this case one fills the complex grid with per-voxel refractive index values using $\chi\Delta_z$ for the material thickness t of Eq. 16, where now χ includes the effects of tilting the zone plate relative to the calculation grid.

In the optic-aligned approach, the calculation grid can be one voxel deep in the beam propagation direction if the thickness of the zone plate t_{zp} is less than or equal to the calculation grid voxel depth Δ_z, or $t_{zp} \leq \Delta_z$. When $t_{zp} > \Delta_z$, or in the case of the wavefield-aligned approach (where one tilts the zone plate relative to the calculation grid), one must propagate the incident wavefield through the calculation grid over multiple voxels in depth. This can be done using the multislice propagation method as noted above; however, in this case one must calculate the optical modulation produced by the first plane in the 3D grid using Eq. 16 but with $t \rightarrow \chi\Delta_z$, and then free space propagation over a distance Δ_z is used to bring the wavefield to the next plane in the calculation grid. This process continues until one has obtained the exit wave at the back side of the calculation grid, after which one can use simple wavefield-aligned free space propagation methods to bring the wave to the focal plane.

For these numerical calculations, the voxel width Δ_x of the calculation grid should be set to some small fraction ϵ_1 of the finest zone width dr_N, such as with $\epsilon_1 = 0.1$. Ideally the pixel depth Δ_z should be reduced in a series of numerical calculations to find how the results asymptotically approach the result obtained with very thin values of Δ_z, but a reasonable estimate can be found by setting the voxel depth to be a fraction ϵ_2 of the depth of focus of the untilted zone plate's focus, with $\epsilon_2 = 0.1$ giving good results [25]. One can obtain a similar estimate using the Klein–Cook parameter Q of [37]

$$Q = \frac{2\pi}{n} \frac{\lambda(\Delta_z)}{d^2}, \tag{19}$$

where n is the mean refractive index (which is $n \simeq 1$ for X rays based on Eq. 2). Values of $Q \lesssim 1$ are adequately described using plane grating diffraction, while the condition $Q \gtrsim 1$ means that volume diffraction effects begin to come into play. If the grating half-period is $b\Delta_r$, one can rearrange Eq. 19 in terms of the slice thickness to find

$$\Delta_{z,Q} = \frac{2nb^2Q}{\pi}\frac{(\Delta_r)^2}{\lambda}. \tag{20}$$

The condition of having $\epsilon_1 = 0.1$ and $\epsilon_2 = 0.1$ corresponds to $Q = 5\pi/(nb^2)$. As an example, if the pixel size is one-fifth the finest zone width dr_N in a Fresnel zone plate, one has $b = 5$ and $Q = \pi/5$, which indeed satisfies $Q \lesssim 1$.

4 Implementation

We have implemented both the optic-aligned and wavefield-aligned approaches using the multislice method [20], with an implementation described in Algorithm 1. This was done for example zone plates for soft x-ray focusing at 0.5 keV, and hard x-ray focusing at 10 keV, with parameters as given in Table 1. Propagation over the short distance Δ_z between slices within the zone plate was accomplished using

$$\psi_d(x, y) = \mathscr{F}^{-1}\{\mathscr{F}\{\psi_s(x, y)\} \odot H(u, v, \Delta_z)\} \tag{21}$$

where $\odot$ represents pointwise multiplication, $\mathscr{F}$ represents a Fourier transform and $\mathscr{F}^{-1}$ its inverse, (x, y) are transverse coordinates in real space and (u, v) in reciprocal space, and

$$H(u, v, \Delta_z) = \exp\left[-i\frac{2\pi\Delta_z}{\lambda}\sqrt{1 - \lambda^2(u^2 + v^2)}\right] \tag{22}$$

is the Fresnel propagation kernel in reciprocal space. For propagation over the longer distance f to the focal spot, we use

$$\psi_d(x_d, y_d) = \frac{if}{\lambda}\{h(x_d, y_d, f) \odot \mathscr{F}\{\psi_s(x_s, y_s) \odot h_s(x_s, y_s, f)\}\} \tag{23}$$

where

$$h(x, y, f) = \exp\left[-i\frac{2\pi}{\lambda}\sqrt{x^2 + y^2 + f^2}\right] \tag{24}$$

is the Fresnel propagation kernel in real space. In the case of longer propagation distances where Eq. 23 is used, the pixel size in the destination plane Δ'_x is given by [25]

$$\Delta'_x = \frac{\lambda\Delta_z}{N\Delta_x}. \tag{25}$$

Use of the appropriate form of wavefield propagation for the distance required avoids aliasing effects [38, 39].

For the optic-aligned approach, we use Algorithm 1 where we first apply a linear phase shift given by Eq. 17 to the illumination wave. In this case, the position of the focal spot shifts by a distance $f\sin(\theta)$ in the output plane, which must be corrected for when extracting the sub-

array containing the focal spot as shown in Algorithm 2. In practice, this method is well suited to simulating soft x-ray zone plates as the focal length and thus spot shift distance is relatively small.

The longer focal length $f = (2r_N\, dr_N)/\lambda$ of hard x-ray zone plates with small λ limits the maximum tilt that can be accommodated, as described by Eq. 18. Therefore with hard x-ray zone plates one is more likely to use the wavefield-aligned approach described above, using partial voxel filling (Fig. 3) to properly represent the tilted zone plate in the refractive index array. The implementation of the wavefield-aligned approach described in Algorithm 3 consists of three steps:

1. To simplify the task of rotatation, we first reduce the size of the optic refractive index array to a small size containing the optic itself. Recall that we use a grid size much larger than the optic size because we want the output plane step size to match the input plane step size of Eq. 25. For the example paramters shown Table 1, this reduces the grid size from 55296^2 to $\approx 15000^2$. The rotation now has to occur on a three dimension grid of size $15\,000 \times 15\,000 \times N_z$, where N_z refers to the number of slices which will be used for propagaton.

Algorithm 1: Optic simulation using the multislice method.

```
/* initialize                                                          */
ψ(x, y) ← 1
/* diffraction within optic                                            */
for n=1,N do
    SliceDiff(n)
    PropShort(Δ_z)
end
/* Propagate exit wave by a focal length f to the focal plane          */
PropLong(f)
Procedure SliceDiff(n)
    /* Apply refractive effect of slice using Eq. 16                   */
    ψ(x, y) = ψ(x, y) ⊙ exp[ i (2πΔ_z/λ) (δ(x, y) + iβ(x, y)) ]
    return
Procedure PropShort(Δ_z)
    /* Free space propagation using Eq. 21 from source s to destination d plane */
    ψ_s(x, y) --F--> Ψ(u, v)
    Ψ(u, v) = Ψ(u, v) ⊙ exp[ −i (2πΔ_z/λ) √(1 − λ²(u² + v²)) ]
    Ψ(u, v) --F^-1--> ψ_d(x, y)
    return
Procedure PropLong(f)
    /* Free space propagation using Eq. 23 from source s to destination d plane */
    ψ'(x, y) = ψ_s(x, y) ⊙ exp[ −i (2πf/λ) √(x_s² + x_s² + f²) ]
    ψ'(x, y) --F--> Ψ'(x, y)
    Ψ_d(x, y) = Ψ'(x, y) ⊙ exp[ −i (2πf/λ) √(x_d² + x_d² + f²) ]
    ψ_d(x, y) = (iΔ_s²/λf) Ψ_d(x, y)
    return
```

Algorithm 2: Algorithm for the optic-aligned approach. Steps described in Algorithm 1 are not re-described here.

```
/* For each angle in range of interest                                  */
for i=1,K do
    /* initialize                                                       */
    AddPhase(θ)
    /* diffraction within optic                                         */
    for n=1,N do
        SliceDiff(n)
        PropShort(Δz)
    end
    /* Propagate exit wave by a focal length f to the focal plane       */
    PropLong(f)
end
Procedure AddPhase(θ)
    /* Apply phase to mimic tilt misalignment as per Eq. 17             */
    ψ(x, y) ← 1
    φx = (2π/λ) tan(θ)x
    ψ(x, y) = ψ(x, y) ⊙ exp[iφx]
    return
```

2. We now have a dataset with dimensions 15 000 × 15 000 × N_Z where the grid size in the plane of optic is different from the grid size along the direction of the beam propagation. Since rotating an isotropic grid is easier than rotating a non-isotropic grid, the grid is "expanded" along the direction of propagation to give $\Delta_Z = \Delta_X$. Rotation is now performed in small batches along the axis of rotation on the isotropic grid. We use libvips [40] to perform the rotation as an affine transform with bilinear interpolation due to its efficiency, parallelism, and low memory needs[1].

3. Finally, the grid is then "collapsed" back to the number of slices N_Z to be used for propagation by a simple scaled summation. The size of the dataset is now back to 15 000 × 15 000 × N_Z. The only difference from the basic optic simulation algorithm is this: at each step of the multi-slice loop, we now extract the refractive index pattern from the HDF5 file and expand the grid size via zero padding. This is followed by the usual multi-slice method of scalar diffraction and near field propagation. The exit wave is finally propagated to the focus.

We chose to implement the above in the Python3 programming language, utilizing the scientific Python stack based upon NumPy [41] and SciPy. Additionally, the package numexpr [42] was used to speed up the pointwise multiplication required by propagation function. The FFT's were performed using FFTW [43] via the Python bindings provided by pyFFTW [44]. We use the HDF5 library[45] via the Python interface h5py[46] to store all datasets with chunking enabled to enable fast I/O. Owing to the nature of scientific Python ecosystem where many packages offer Python interfaces for software packages (such as FFTW, HDF5, libvips, etc.) with underlying code in C or Fortran, care was taken to install them with the Intel Compiler Collection using the spack[47] package manager. This was done to ensure optimal performance on the workstation. Our code is available at https://github.com/s-sajid-ali/zone_plate_testing.

All calculations were performed on a workstation with two Intel Xeon E5-2620 v4 processors and 512 GB RAM. Because the large array size exceeded their available memory, GPUs were not used. A typical optic-aligned simulation (for $Q = 3.33$, $\theta = 2.5°$) took

[1] https://github.com/libvips/libvips/wiki/Why-is-libvips-quick

approximately 30 minutes, and a typical wavefield-aligned simulation (for $Q = 3.33$, $\theta = 2.5°$) took approximately 150 minutes.

Algorithm 3: Wavefield-aligned approach. Steps described in Algorithm 1 are not re-described here.

```
/* Reduce the pattern down to essential area.                          */
Reduce (pattern)
/* For each angle in range of interest                                 */
for i=1,K do
    Rotate (pattern_reduced)
    /* For each slice in a zone plate at a given tilt misalignment perform
       multislice simulation                                           */
    for n=1,N do
        Extract (pattern_reduced)
        SliceDiff(n)
        PropShort(Δz)
    end
    PropLong(f)
end
Procedure Reduce (pattern)
    /* Extract relevant part of zone plate                             */
    /* choose and save appropriate parameters viz.  number of slices, step size
       along propagation direction                                     */
    pattern →pattern_reduced
    return
Procedure Rotate (pattern_reduced)
    /* Rotate zone plate pattern                                       */
    /* Expand the number of slices along direction of propagation to form an
       isotropic three dimensional grid.                               */
    pattern_reduced --Expand--> pattern_isometric
    /* Rrotate along axis of rotation                                  */
    pattern_isometric --Rotation--> pattern_isometric
    /* reduce number of slices to number of slices for propagation.    */
    pattern_isometric --Collapse--> pattern_reduced
    return
Procedure Extract (pattern_reduced)
    /* Extract zone plate pattern at slice, expand back to grid size neede for
       propagation.                                                    */
    pattern_reduced →pattern
    return
```

5 Simulation results

We have carried out the above procedures to evaluate the focusing properties of two zone plates with $dr_N = 21$ nm outermost zone width and a diameter of $2r_N = 58.9$ μm: one for focusing 0.5 keV soft X rays (such as are used for imaging in the "water window" between the carbon and oxygen K absorption edges [48]), and one for focusing 10 keV hard X rays (such as are used in scanning fluorescence x-ray microscopes). Further parameters for these zone plates are given in Table 1. In each case, we carried out simulations for values of the Klein–Cook paraameter Q of 0.33, 3.33, and 10 to see the role that waveguide effects play in tilted zone plate focusing. In addition to showing images (Figs. 5 and 6) and plots (Figs. 7) of the intensity around the focal spot region, we show in Figs. 8 and 9 two other measures of zone plate performance:

1. Diffraction efficiency: this is the fraction of energy in the vicinity of the $m = 1$ first order focus, even if the focal spot is of poor quality. For a zone plate with a small value of the Klein–Cook parameter Q, the expected value can be calculated using scalar diffracton theory and knowledge of the x-ray refractive index [6].
2. Strehl ratio: this is the ratio of the peak intensity in the focal region at a given tilt angle relative to the intensity at zero tilt angle, for a given zone plate thickness.

Together, these measures show the effects of tilt on zone plate performance.

Consider first the case of the 0.5 keV soft x-ray zone plate with no tilt ($\theta = 0°$). Because the values of $\delta = 0.00474$ and $\beta = 0.00465$ for gold are quite similar at 0.5 keV, Eq. 1 does not lead to the maximum scalar diffraction efficiency: a thickness of $t_{zp} = 0.191$ μm (with $Q = 1.67$) gives a scalar diffraction efficiency of 0.117 whereas $t_{zp,opt} = 0.096$ μm (with $Q = 0.86$) gives a calculated efficiency of 0.087. Thus the result shown for $Q = 0.33$ has reduced diffraction efficiency (Fig. 8), but has an Airy focus profile as expected from scalar diffraction theory (Figs. 5 and 7). At higher Q values, Fig. 8 shows that the diffraction efficiency with waveguide effects included exceeds the scalar efficiency, with $Q = 3.33$ providing higher efficiency than $Q = 10$. At the same time, the waveguide effects at high Q mean that the focus profile is degraded, as can be seen in Figs. 5 and 7.

The behavior of the 0.5 keV soft x-ray zone plates upon tilt depends on the thickness and thus the value of Q. For the thin zone plate with $Q = 0.33$, the diffraction efficiency is unaffected by tilt (no waveguide effects are involved), but the focal profile degrades as the tilt θ is increased (Fig. 5). For the thicker zone plates, the diffraction efficiency begins to drop off as one approaches the Bragg angle $\theta_B(r_N)$ for the outermost zones. In addition, the net path length error ℓ_l' of Eq. 10 between axial and lower marginal rays matches the Rayleigh quarter wave limit at an angle of $\theta_l = 0.548°$, which is the tilt angle where one starts to see a reduction in the Strehl ratio.

The behavior of the 10 keV hard x-ray zone plate upon tilt is rather different. Here the diffraction efficiency shows a sharp increase as the tilt angle θ matches the outermost zone Bragg angle $\theta_B(r_N)$ (Eq. 3) for the $Q = 3.33$ case, whereas the $Q = 10$ case shows a decrease in focusing efficiency for any angle other than normal incidence, with a dropoff characterized by $\theta_B(r_N)$.. Also, Fig. 2 shows that there is very little ℓ_c' offset to the $\ell_a'\theta^2$ term in the expression for the net path length error of Eq. 10, so that the tilt limit of $\theta_l = 1.191°$ from Eq. 13 nicely describes the decrease in diffraction efficiency and Strehl ratio observed as function of zone plate tilt θ.

6 Conclusion

We have systematically studied the effect of tilt at different x-ray energies as a function of thickness and number of zones on a zone plate. The tilt limit of θ_l (Eq. 13) that one arrives at by using the axial and lower marginal rays and the Rayleigh quarter wave criterion provides a good estimate of the tilt misalignment tolerance of thin zone plates. This analysis indicates that zone plates used for focusing 0.5 keV soft X rays are more demanding of proper tilt alignment than are zone plates used for 10 keV hard X rays. As the zone plate thickness is increased to the point where waveguide effects begin to be important (that is, as the Klein–Cook parameter Q of the outermost zones approaches values of 1 or more; see Eq. 19), then the allowable tilt is greatly reduced, and is better characterized by the Bragg angle θ_B of the outermost zones as given by Eq. 3.

The calculations shown here have been for the properties of a focal spot produced by plane wave illumination, which is representative of the case of scanning x-ray microscopes. In

full-field or transmission x-ray microscopes (TXMs), high optical magnifications are employed due to the large pixel size of common x-ray image detectors [3]. As a result, a point object on axis essentially produces a plane wave from the objective zone plate to the detector. In other words, the principle of reciprocity [49, 50, 51] relates the light source in scanning microscopy to the detector in full-field microscopy. Because of this, the results shown here are directly applicable to TXM imaging of objects near the optical axis. Further studies should be carried out to consider the degree to which the tilt of 2D objective zone plates affects off-axis imaging points, which could degrade the usable field of view beyond what one would expect for a non-tilted zone plate [52, 3].

Acknowledgement

This research used resources of the Advanced Photon Source, a U.S. Department of Energy (DOE) Office of Science User Facilities operated for the DOE Office of Science by Argonne National Laboratory under Contract No. DE-AC02-06CH11357. We thank the National Institute of Mental Health, National Institutes of Health, for support under grant R01 MH115265. The authors would like to thank Kenan Li and Michael Wojcik for helpful discussions.

References

[1]. Michette AG. X-ray microscopy. Reports on Progress in Physics, 51:1525–1606, 1988.

[2]. Urquhart Stephen and Hitchcock Adam P. Proceedings of the 14th international conference on x-ray microscopy (XRM2018) Microscopy and Microanalysis, 24(S2):f1–f20, 8 2018.

[3]. Jacobsen Chris. X-ray Microscopy. Cambridge University Press, Cambridge, UK, 2019.

[4]. Myers Ora E. Jr. Studies of transmission zone plates. American Journal of Physics, 19(6):359–365, 1951.

[5]. Baez Albert V. A study in diffraction microscopy with special reference to x-rays. Journal of the Optical Society of America, 42(10):756–762, 1952.

[6]. Kirz J. Phase zone plates for x-rays and the extreme UV. Journal of the Optical Society of America, 64(3):301–309, 1974.

[7]. Henke BL, Gullikson EM, and Davis JC. X-ray interactions: Photoabsorption, scattering, transmission, and reflection at E=50–30,000 eV, Z=1–92. Atomic Data and Nuclear Data Tables, 54:181–342, 1993.

[8]. Chao W, Fischer P, Tyliszczak T, Rekawa S, Anderson E, and Naulleau P. Real space soft x-ray imaging at 10 nm spatial resolution. Optics Express, 20(9):9777–9783, 2012. [PubMed: 22535070]

[9]. Döring F, Robisch AL, Eberl C, Osterhoff M, Ruhlandt A, Liese T, Schlenkrich F, Hoffmann S, Bartels M, Salditt T, and Krebs HU. Sub-5 nm hard x-ray point focusing by a combined Kirkpatrick-Baez mirror and multilayer zone plate. Optics Express, 21(16):19311–19323, 2013. [PubMed: 23938848]

[10]. Mohacsi Istvan, Vartiainen Ismo, Rösner Benedikt, Guizar-Sicairos Manuel, Guzenko Vitally A, McNulty Ian, Winarski Robert, Holt Martin V, and David Christian. Interlaced zone plate optics for hard x-ray imaging in the 10 nm range. Scientific Reports, 7:43624, 2017.

[11]. Chang Chieh and Sakdinawat Anne. Ultra-high aspect ratio high-resolution nanofabrication for hard x-ray diffractive optics. Nature Communications, 5:4243, 6 2014.

[12]. Parfeniukas Karolis, Giakoumidis Stylianos, Vogt Ulrich, and Akan Rabia. High-aspect ratio zone plate fabrication for hard x-ray nanoimaging. Proceedings SPIE, 10386:103860S, 2017.

[13]. Li Kenan, Wojcik Michael J., Divan Ralu, Ocola Leonidas E., Shi Bing, Rosenmann Daniel, and Jacobsen Chris. Fabrication of hard x-ray zone plates with high aspect ratio using metal-assisted chemical etching. Journal of Vacuum Science & Technology B, 35(6):06G901, 2017.

[14]. Werner Stephan, Rehbein Stefan, Guttmann Peter, and Schneider Gerd. Three-dimensional structured on-chip stacked zone plates for nanoscale x-ray imaging with high efficiency. Nano Research, 7(4):528–535, 2014.

[15]. Maser Jörg and Schmahl Günter. Coupled wave description of the diffraction by zone plates with high aspect ratios. Optics Communications, 89(2-4):355–362, 1992.

[16]. Schneider Gerd. Zone plates with high efficiency in high orders of diffraction described by dynamical theory. Applied Physics Letters, 71(16):2242–2244, 1997.

[17]. Schneider G, Rehbein S, and Werner S. Volume effects in zone plates In Erko Alexei, Idir Mourad, Krist Thomas, and Michette Alan G, editors, Modern Developments in X-ray and Neutron Optics, pages 137–171. Springer, 2008.

[18]. Rehbein S, Heim S, Guttmann P, Werner S, and Schneider G. Ultrahigh-resolution soft-x-ray microscopy with zone plates in high orders of diffraction. Physical Review Letters, 103(11):110801, 2009. [PubMed: 19792359]

[19]. Yan Hanfei, Conley Ray, Conley Raymond P, Bouet Nathalie, and Chu Yong S. Hard x-ray nanofocusing by multilayer Laue lenses. Journal of Physics D, 47(26):263001, 6 2014.

[20]. Cowley JM and Moodie AF. The scattering of electrons by atoms and crystals. I. A new theoretical approach. Acta Crystallographica, 10(10):609–619, 10 1957.

[21]. Ishizuka K and Uyeda N. A new theoretical and practical approach to the multislice method. Acta Crystallographica A, 33(5):740–749, 9 1977.

[22]. Van Roey J, van der Donk J, and Lagasse PE. Beam-propagation method: analysis and assessment. Journal of the Optical Society of America, 71(7):803–810, 7 1981.

[23]. Kopylov Yuri V, Popov Alexei V, and Vinogradov Alexei V. Diffraction phenomena inside thick Fresnel zone plates. Radio Science, 31(6):1815–1822, 11 1996.

[24]. Kurokhtin Alexei N and Popov Alexei V. Simulation of high-resolution x-ray zone plates. Journal of the Optical Society of America, A, 19(2):315–324, 2 2002.

[25]. Li Kenan, Wojcik Michael J, and Jacobsen Chris. Multislice does it all – calculating the performance of nanofocusing x-ray optics. Optics Express, 25(3):185–194, 2017.

[26]. Li Kenan and Jacobsen Chris. More are better, but the details matter: combinations of multiple Fresnel zone plates for improved resolution and efficiency in x-ray microscopy. Journal of Synchrotron Radiation, 25(4):1048–1059, 2018. [PubMed: 29979166]

[27]. Young M. Zone plates and their aberrations. Journal of the Optical Society of America, 62(8):972–976, 1972.

[28]. Ali Syed Sajid, Li Kenan, Wojcik Michael J, and Jacobsen Chris. Zone plate performance as a function of tilt analyzed via multislice simulations. Microscopy and Microanalysis, 24(S2):302–303, 8 2018.

[29]. David C, Nöhammer B, and Ziegler E. Wavelength tunable diffractive transmission lens for hard x rays. Applied Physics Letters, 79(8):1088–1090, 2001.

[30]. Ocola Leonidas Ernesto, Maser Joerg, Vogt Stefan, Lai Barry, Divan Ralu, and Stephenson Gregory B.. Tapered tilted linear zone plates for focusing hard x-rays. Proceedings SPIE, 5539:165–173, 2004.

[31]. Maser Jörg, Stephenson GB, Vogt Stefan, Yun Wenbing, Macrander Albert T, Kang Hyon Chol, Liu C, and Conley R. Multilayer Laue lenses as high-resolution x-ray optics. Proceedings SPIE, 5539:185–194, 10 2004.

[32]. Yan Hanfei, Maser Jörg, Macrander Albert T, Shen Qun, Vogt Stefan, Stephenson G Brian, and Kang Hyon Chol. Takagi-Taupin description of x-ray dynamical diffraction from diffractive optics with large numerical aperture. Physical Review B, 76(11):115438, 9 2007.

[33]. Conley Raymond P, Liu Chian, Qian Jun, Kewish Cameron M, Macrander Albert T, Yan Hanfei, Kang Hyon Chol, Maser Jörg, and Stephenson G Brian. Wedged multilayer Laue lens. Review of Scientific Instruments, 79(5):053104, 5 2008. [PubMed: 18513058]

[34]. Delen N and Hooker B. Free-space beam propagation between arbitrarily oriented planes based on full diffraction theory: a fast Fourier transform approach. Journal of the Optical Society of America A, 15(4):857–867, 4 1998.

[35]. Matsushima Kyoji. Shifted angular spectrum method for off-axis numerical propagation. Optics Express, 18(17):18453–18463, 2010. [PubMed: 20721240]

[36]. Yamamoto Kenji, Ichihashi Yasuyuki, Senoh Takanori, Oi Ryutaro, and Kurita Taiichiro. Calculating the Fresnel diffraction of light from a shifted and tilted plane. Optics Express, 20(12):12949–12958, 2012. [PubMed: 22714322]

[37]. Klein WR and Cook BD. Unified approach to ultrasonic light diffraction. IEEE Transactions on Sonics and Ultrasonics, 14(3):123–134, 7 1967.

[38]. Voelz David G and Roggemann Michael C. Digital simulation of scalar optical diffraction: revisiting chirp function sampling criteria and consequences. Applied Optics, 48(32):6132–6142, 11 2009. [PubMed: 19904309]

[39]. Li Kenan and Jacobsen Chris. Rapid calculation of paraxial wave propagation for cylindrically symmetric optics. Journal of the Optical Society of America A, 32(11):2074–2081, 2015.

[40]. Martinez K and Cupitt J. VIPS - a highly tuned image processing software architecture. In IEEE International Conference on Image Processing 2005, volume 2, pages II–574, Sep. 2005.

[41]. Oliphant Travis E.. Python for scientific computing. Computing in Science & Engineering, 9(3):10–20, 2007.

[42]. McLeod Robert, Alted Francesc, Valentino Antonio, de Menteno Gaëtan, Wiebe Mark, Gohlke Christoph, Bedini Andrea, Mamrehn, Techtonik Anatoly, Erb Stephan, Shadchin Alexander, Bunin Aleks, Kooij Tom, Pavlyk Oleksandr, Jelloul Mahdi Ben, Garrison Lehman, Hurtado David Menéndez, Carey CJ, Sarahan Mike, Cox David, Plesivččak Zoran, Borgdorff Joris, Courbet Clement, Dickinson Mark, Leitao Breno, de Laat Arne, Pitrou Antoine, Portnoy Andrey, Ortega Alvaro Lopez, and Böhn Alexander. pydata/numexpr: NumExpr v2.6.9, 12 2018.

[43]. Frigo M and Johnson SG. The design and implementation of FFTW3. Proceedings of the IEEE, 93(2):216–231, 2 2005.

[44]. Gomersall Henry. pyfftw, 6 2016.

[45]. The HDF Group. Hierarchical Data Format, version 5, 1997–2019. http://www.hdfgroup.org/HDF5/.

[46]. HDF5 for Python. https://www.h5py.org/.

[47]. Gamblin T, LeGendre M, Collette MR, Lee GL, Moody A, de Supinski BR, and Futral S. The Spack package manager: bringing order to HPC software chaos. In SC15: International Conference for High-Performance Computing, Networking, Storage and Analysis, pages 1–12, Los Alamitos, CA, USA, 11 2015 IEEE Computer Society.

[48]. Wolter H. Spiegelsysteme streifenden Einfalls als abbildende Optiken für Röntgenstrahlen. Annalen der Physik, 10:94–114, 286, 1952.

[49]. Zeitler E and Thomson MGR. Scanning transmission electron microscopy. I. Optik, 31(3):258–280, 1970.

[50]. Zeitler E and Thomson MGR. Scanning transmission electron microscopy. II. Optik, 31(4):359–366, 1970.

[51]. Engel A. The principle of reciprocity and its application to conventional and scanning dark field electron microscopy. Optik, 41(2):117–126, 1974.

[52]. Jacobsen Chris, Howells Malcolm R, and Warwick Tony. Zone-plate x-ray microscopy In Hawkes Peter W and Spence John C H, editors, Springer Handbook of Microscopy, chapter 23, pages 1145–1204. Springer International Publishing, Cham, 2019.

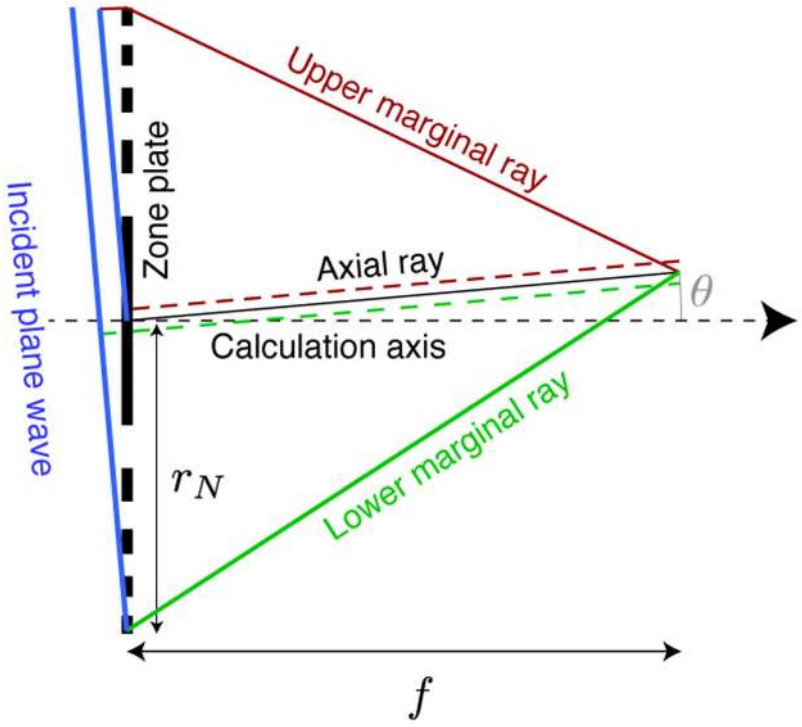

Figure 1:

Geometry of a Fresnel zone plate with an incident plane wave inclined by an angle θ relative to the zone plate's axis. The zone plate's radius is r_N and the focal length is f. We consider optical path length differences between the three rays labeled upper marginal ray, axial ray, and lower marginal ray. The calculation of the upper marginal ray relative to the axial ray is for a wavefield centered on the axis (the axial ray limits are indicated by the dashed red line), while for the lower marginal ray relative to the axial ray it is for a wavefield intersecting the bottom edge of the zone plate (indicated by a dashed green line).

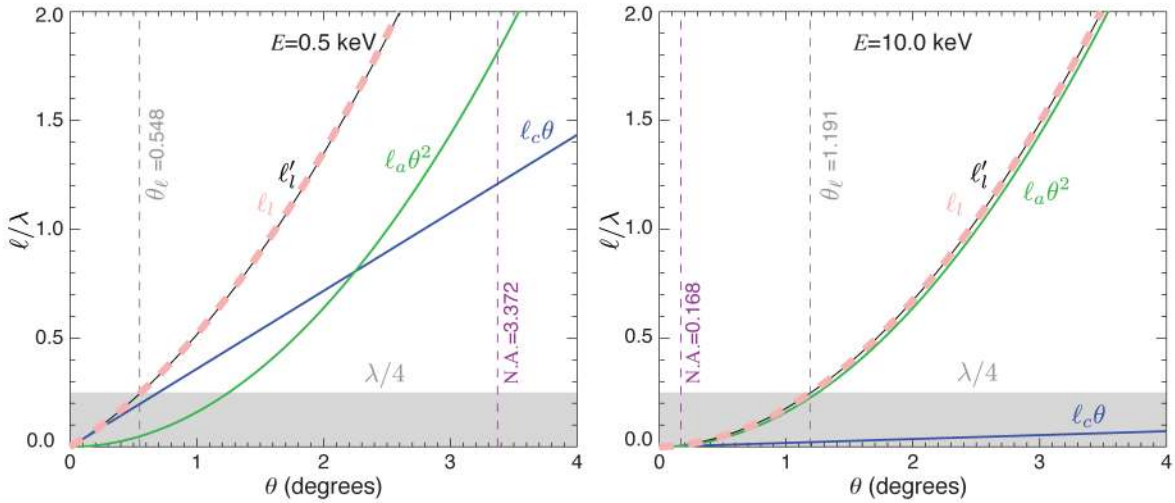

Figure 2:

Optical path length errors ℓ (shown as a fraction of the wavelength λ) between the lower marginal ray and the axial ray of a Fresnel zone plate as a function of tilt θ. The exact path length error ℓ'_l of Eq. 8 is shown as a solid black line, along with the approximate expression terms $\ell_c\theta$ (coma) and $\ell_a\theta^2$ (astigmatism and field curvature) which together add up to ℓ_l in Eq. 10. These terms are shown at left for a soft x-ray zone plate (E = 0.5 keV), and at right for hard x-ray zone plate (E = 10 keV). The same radius r_N = 29.4 μm and outermost zone width dr_N = 21 nm was used in both cases in accordance with Table 1, leading to numerical apertures of N.A. = 3.372 degrees at 0.5 keV and N.A. = 0.168 degrees at 10 keV as indicated in the plots. The λ/4 path length of the Rayleigh quarter wave criterion is also indicated as a gray box, along with the value of θ_l from Eq. 13 where ℓ_l = λ/4.

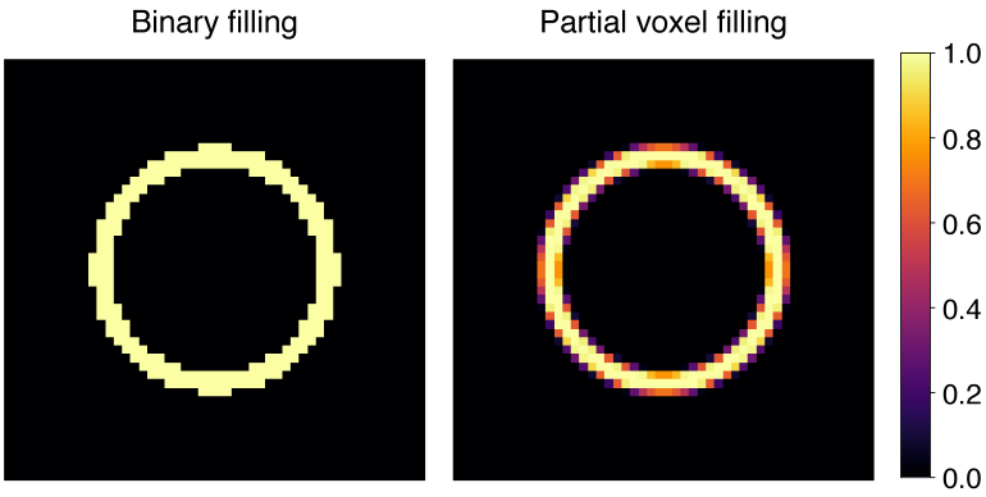

Figure 3:

Example of partial filling of calculation grid voxels with Fresnel zone plate zones. In the example at left, voxels are either fully filled corresponding to a zone plate thickness t_{zp}, or left empty, leading to aliasing errors. In the example at right, each voxel is filled corresponding to a thickness of $\chi\Delta_z$, where χ is the fraction of the voxel that contains zone plate material. This partial voxel filling approach has been shown to work well in multislice propagation simulations [25].

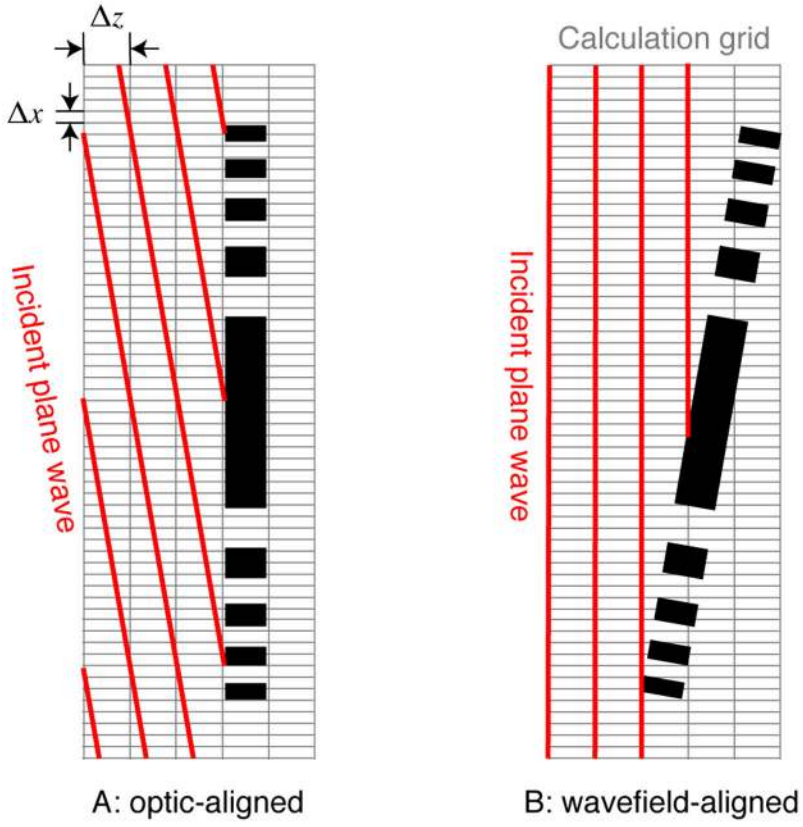

Figure 4:

Alternative approaches for calculating plane wave propagation through Fresnel zone plates that are tilted with respect to the plane wave's direction of travel. In the tilted illumination approach (A), the zone plate is aligned to the calculation grid axis and the incident wave is created with a position dependent tilt φ_x as given by Eq. 17. In the tilted zone plate approach (B), the zone plate is mapped onto the calculation grid by filling in the refractive index difference from vacuum into each grid in proportion to the fractional volume occupied by a zone. In the method at left, the zone plate focal spot can wind up outside the calculation grid for large tilt angles, while in the method at right one has to deal with partial voxel filling. One can choose to have non-isotropic voxels and an asymmetric total volume, based on the choice of the transverse voxel size Δ_x and transverse number of voxels N_x, and longitudinal voxel size Δ_z and longitudinal number of voxels N_z.

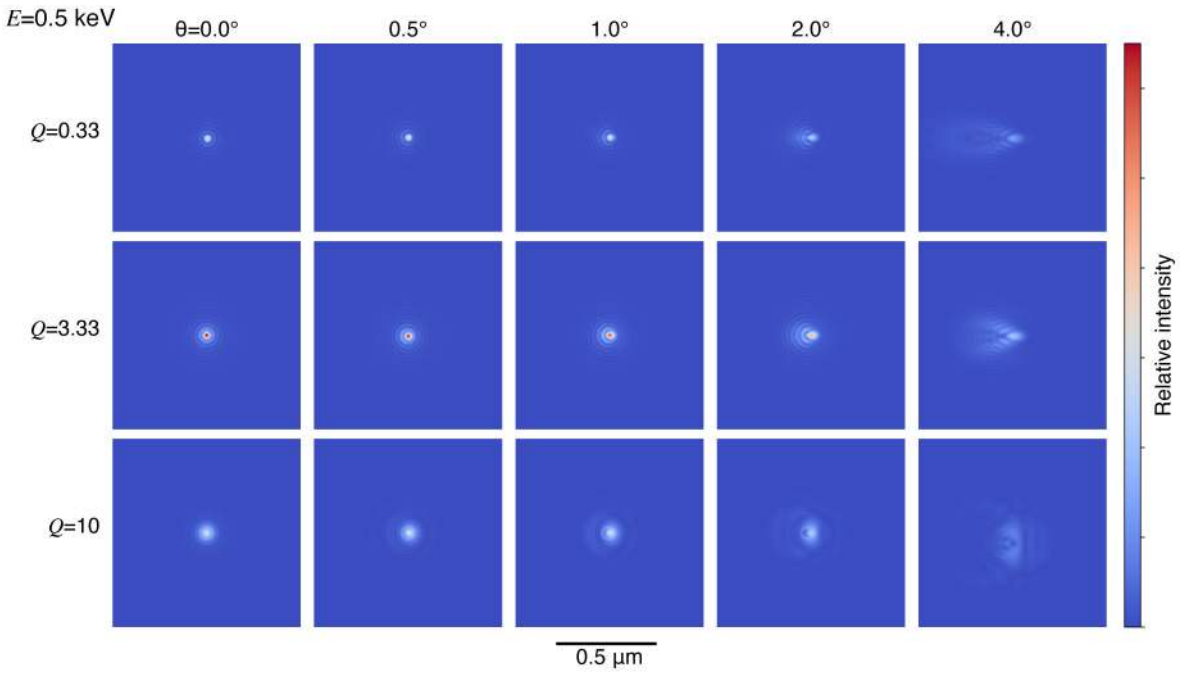

Figure 5:

Focal spot intensity images for a 0.5 keV soft x-ray zone plate (parameters given in Table 1) as a function of tilt angle θ. For the zone plate with a Klein–Cook parameter of $Q = 0.33$ such that waveguide effects are not present, one sees the expected small focal spot at 0° tilt, but by the time the tilt has been increased to 2° significant coma aberrations appear. For thicker zone plates with $Q = 3.33$ and $Q = 10$, waveguide effects begin to degrade the focal spot and reduce its intensity, as shown in Fig. 8.

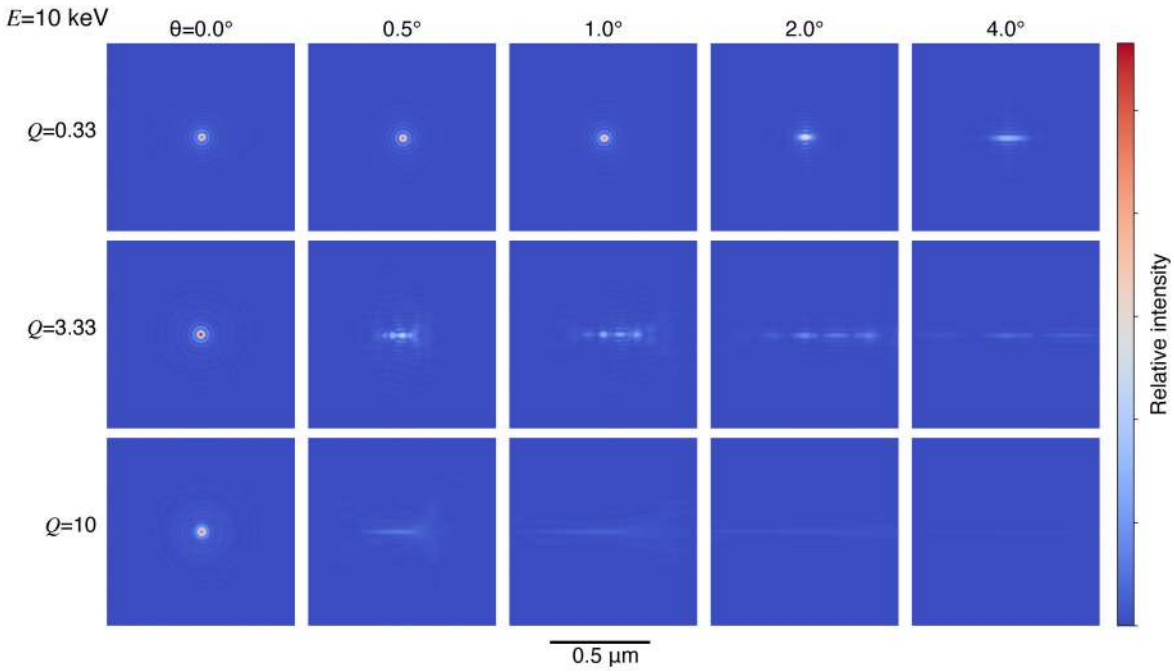

Figure 6:

Focal spot intensity images for a 10 keV hard x-ray zone plates (parameters given in Table 1) as a function of tilt angle θ. For the zone plate with a Klein–Cook parameter of $Q = 0.33$ such that waveguide effects are not present, one sees the expected small focal spot at 0° tilt, with astigmatism beginning to degrade the focal spot by the time the tilt has been increased to 2°. For thicker zone plates with $Q = 3.33$ and $Q = 10$, waveguide effects degrade the focus even at small tilt angles. The diffraction efficiency and Strehl ratio are shown in Fig. 9.

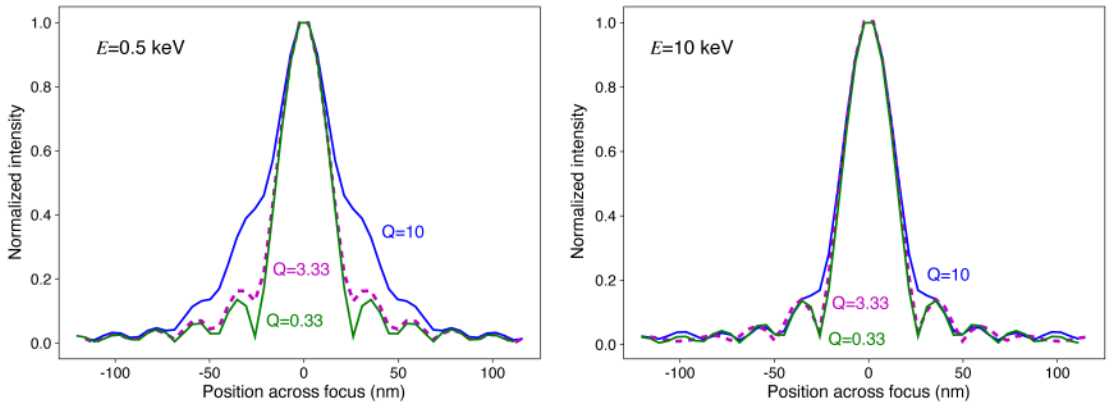

Figure 7:

Focal spot profile at 0.5 keV and 10 keV for $Q = 0.33$, 3.33, and 10 with no tilt ($\theta = 0$). This shows how waveguide effects in the zone plate begin to alter the exit wave from that which would produce the finest focus, so that the spatial resolution is degraded. This degradation of the focus could in principle be corrected for by accouting for volume diffraction effects in the optic's design, such as by a radially-varying tilt of zones to be on the Bragg condition of Eq. 3 [15]. However, this is difficult to achieve using normal top-down nanofabrication methods.

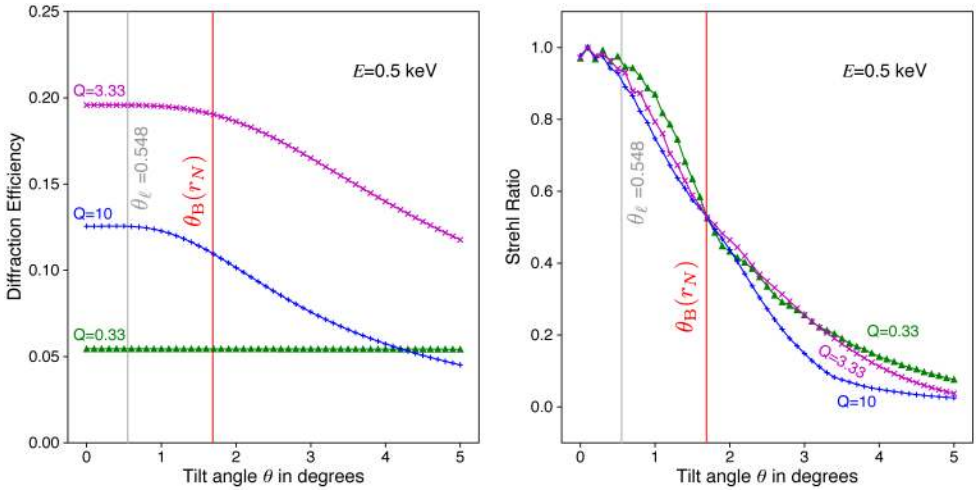

Figure 8:

Diffraction efficiency, and Strehl ratio, for a 0.5 keV soft x-ray zone plate (parameters given in Table 1) as a function of tilt θ. This is done for zone plates with three different thicknesses corresponding to the indicated values of the Klein–Cook parameter Q. As can be seen, the Strehl ratio degrades at tilts beyond the $\theta_l = 0.548°$ limit calculated using Eq. 13, showing a loss of peak focal intensity. Also shown is the Bragg angle $\theta_B(r_N)$ for the outermost zones, as given by Eq. 3.

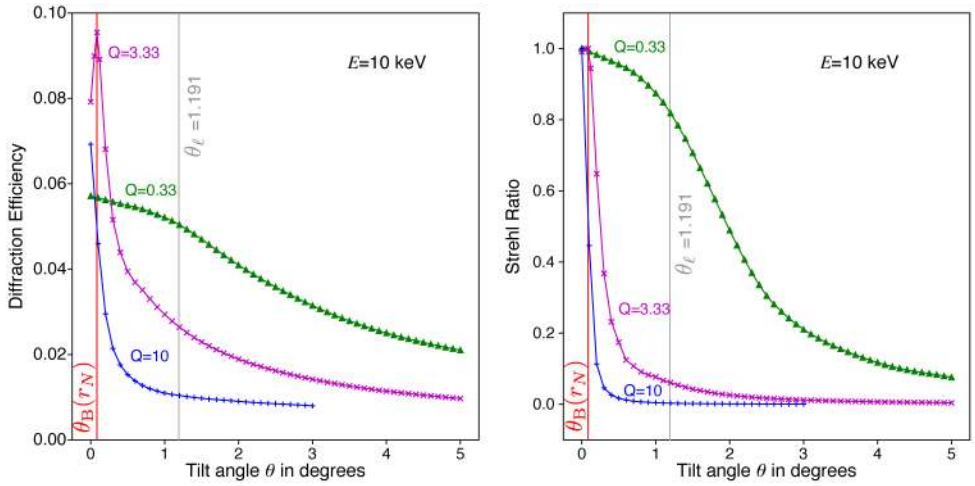

Figure 9:

Diffraction efficiency, and Strehl ratio, for a 10 keV hard x-ray zone plate (parameters given in Table 1) as a function of tilt θ. This is done for zone plates with three different thicknesses corresponding to the indicated values of the Klein–Cook parameter Q. For hard x-ray zone plates with larger values of Q such that volume diffraction effects begin to be revealed, one can see a strong peak in the diffraction efficiency near the Bragg angle $\theta_B(r_N)$ for the outermost zones, as given by Eq. 3. For the thinner, $Q = 0.33$ zone plate, the tilt limit estimate of $\theta_l = 1.1961°$ given by Eq. 13 provides a reasonable indicator of the tilt tolerance, while the thicker zone plates with higher values of Q show a loss of performance due to waveguide effects at much smaller tilt angles.

Table 1:

Parameters used for tilted zone plate calculations. The zone material is assumed to be gold. The Klein–Cook parameter Q is described in Eq. 19.

Parameter \ Regime	Soft X ray	Hard X ray
Photon energy	0.5 keV	10 keV
Outermost zone width dr_N	21.09 nm	21.07 nm
Diameter $2r_N$	58.90 μm	58.88 μm
Pixels N_x	55,296	55,296
Input array pixel size Δ_x	4.73 nm	4.73 nm
Output array pixel size Δ'_x	4.73 nm	4.74 nm
Focal length f	0.5 mm	10 mm
Numerical aperture N.A. (Eq. 12)	3.372°	0.168°
Bragg tilt angle for outermost zones $\theta_B(r_N)$ (Eq. 3)	1.687°	0.084°
Aberration tilt limit θ_l (Eq. 13)	0.548°	1.191°
Max tilt θ_f (Eq. 18) for using the optic-aligned calculation approach	10.90°	0.75°
Optimum thickness $t_{zp,opt}$ (Eq. 1)	0.098 μm	1.975 μm
t_{zp} for $Q = 0.333$	0.038 μm	0.759 μm
t_{zp} for $Q = 3.333$	0.381 μm	7.594 μm
t_{zp} for $Q = 10$	1.142 μm	22.782 μm